The Astrophysical Journal Letters, 932:L21 (8pp), 2022 June 20 https://doi.org/10.3847/2041-8213/ac75c3

Remarkable Correspondence of the Sagittarius A* Submillimeter Variability with a Stellar-wind-fed Accretion Flow Model

Lena Murchikova[1], Christopher J. White[2], and Sean M. Ressler[3]
[1] Institute for Advanced Study, 1 Einstein Drive, Princeton, NJ 08540, USA; lena@ias.edu
[2] Department of Astrophysical Sciences, Princeton University, Peyton Hall, Princeton, NJ 08544, USA; cjwhite@princeton.edu
[3] Kavli Institute for Theoretical Physics, University of California Santa Barbara, Kohn Hall, Santa Barbara, CA 93107, USA; smressle@ucsb.edu
Received 2022 April 13; revised 2022 May 31; accepted 2022 June 1; published 2022 June 17

Abstract

We compare the 230 GHz near-horizon emission from Sagittarius A* to simulations representing three classes of accretion flows. Using the structure function to capture the variability statistics of the light curve, we find a noticeable discrepancy between the observations and models based on torus-fed accretion disks, whether those disks bring in a small or large amount of net magnetic flux. On the other hand, the simulations that are fed more realistically by stellar winds match the observed structure function very well. We describe the differences between models, arguing that feeding by stellar winds may be a critical component in constructing theoretical models for accretion in the Galactic Center.

Unified Astronomy Thesaurus concepts: Supermassive black holes (1663); Low-luminosity active galactic nuclei (2033); Galactic center (565); Magnetohydrodynamics (1964); Astrophysical fluid dynamics (101); Astrophysical black holes (98); Accretion (14); General relativity (641); Stellar winds (1636); Magnetohydrodynamical simulations (1966)

1. Introduction

Sagittarius A* (Sgr A*) is the closest supermassive black hole to us and is our best hope to study near-horizon phenomena. The peak of its electromagnetic emission is in the submillimeter (submm) range (around 230 GHz; Genzel et al. 2010), and this emission is currently one of the key probes of the near-horizon physics (via, e.g., the Event Horizon Telescope, Event Horizon Telescope Collaboration et al. 2019), and hence understanding its properties is critically important for the whole field to move forward. The submm emission is particularly useful for comparison of observations with simulations because other observational probes of the near-horizon physics (e.g., the NIR Gravity Collaboration et al. 2019, 2020 emission and X-rays Neilsen et al. 2015) are likely connected to high-energy, nonthermal particle acceleration, a process that involves small-scale plasma physics not captured in global accretion simulations.

Two important and complimentary ways to analyze this submm emission are variability studies and black hole imaging studies. Imaging highlights spatial information while typically averaging data in time. Variability analyses highlight temporal evolution while often discarding spatial information. Therefore, in order to obtain a complete picture of black hole/accretion physics, both sets of analysis are required.

The behavior of Sgr A*'s submm flux is not yet fully explained by models. In this work, we analyze the submm variability of Sgr A* on scales between about 10 s and about 200 minutes. We compare observational results (Dexter et al. 2014; Murchikova & Witzel 2021; Witzel et al. 2021) with simulations (Ressler et al. 2020; White et al. 2020). Our numerical models include the following:

(i) SANE torus. A standard and normal evolution (SANE) accretion flow fed by torus initial conditions from White et al. (2020), with a magnetic field with no large-scale net vertical flux.
(ii) MAD torus. A magnetically arrested disk (MAD) accretion flow fed by torus initial conditions, with a large net vertical flux in the inner region.
(iii) MAD winds. Two accretion flows fed by stellar winds from Ressler et al. (2020), both of which naturally become MADs.

We identify an accretion flow model that describes Sgr A* variability nearly perfectly. This model (MAD winds) traces accretion from stellar winds at parsec scales down to the event horizon.

As a measure of Sgr A* variability, we use the intrinsic structure function ($\mathcal{SF}$) defined in Murchikova & Witzel (2021) as an extension of the standard structure function definition in the case where observational uncertainties are present:

$$\mathcal{SF}(\tau) = \sqrt{\frac{1}{N_\tau}\sum\nolimits_{\rm pairs}(F(t+\tau) - F(t))^2 - 2\sigma_{\rm obs}^2}. \quad (1)$$

Here, τ is the time lag, $F(t)$ is the flux at time t, N_τ is the number of pairs of points separated by the time interval τin the data, the summation runs over all such pairs, and $\sigma_{\rm obs}$ is the rms observational uncertainty. In the case of simulated variability, the observational uncertainties are absent ($\sigma_{\rm obs} = 0$). For brevity, throughout the text, we simply refer to $\mathcal{SF}$ as the structure function.

In this work, we focus on the shape of the structure function only and treat its absolute value as a normalization factor. There are two key reasons for this approach. First, we observe a general trend in Sgr A* structure functions calculated with different parts of the data sets: the shapes of the $\mathcal{SF}$ (within the range of timescales τ where the results are statistically reliable) are the same, but the values are offset from each other by a

constant multiplicative factor varying from observation to observation. Second, the available light-curve data are quite varied in origin, value of observational uncertainties, available cadence, and epoch sampling. On long timescales, $\tau \geqslant 25$ minutes, the structure function is dominated by data observed during various epochs between 2009 and 2017. This samples the average value of the long-timescale structure function better than a single continuous light curve covering 30–56 hr. On short timescales, $\tau < 25$ minutes, the observational data are dominated by the data set observed in 2019 with by far the highest cadence and sensitivity. The simulated data on short timescales ($\tau < 3$ minutes) are calculated using high-cadence subsamples of the simulated data. Hence, the short-timescale part of the structure function is not as well sampled as the long-timescale one in both observations and simulations. An offset in the absolute value of the structure functions calculated on short and long timescales or from observational and simulational data may be affected by a particular data sample available, rather than be the internal property of the source or the model (see, e.g., Figure 2 in Murchikova & Witzel 2021).

Taking into account the above observation and the fact that the shape of the structure function seems to persist from independent sample to independent sample, unlike its absolute value, we focus our comparison on the shape of the structure function. We provide the absolute values via normalization factors under each structure function plot.

This paper is organized as follows. We describe the observational data set and construction of the structure function in Section 2. In Section 3, we cover the simulations in more detail. Section 4 describes the process by which we extract submm variability from the simulations. Our analysis follows in Section 5, and we conclude in Section 6. In Appendix, we demonstrate properties of structure functions with simple models.

2. Observational Data

We use observational data sets from Murchikova & Witzel (2021), Witzel et al. (2021), and Dexter et al. (2014). The data were obtained at the frequency of about 230 GHz with the Atacama Large Millimeter/submillimeter Array (ALMA), the Submillimeter Array (SMA), and Combined Array for Research in Millimeter-wave Astronomy (CARMA) between 2009 and 2019. Detailed descriptions of the observations and the data reduction can be found in the corresponding papers. We reanalyze the ALMA data from project 2018.1.01124.S (PI Murchikova) described in Murchikova & Witzel (2021). We update the light-curve extraction procedure, which allows us to obtain the timestamps with decimal second accuracy. The rest of the data analysis and the data reduction are unchanged.

To construct the structure function at timescales $\tau \leqslant 200$ s, we use only the lowest-noise part of the Murchikova and Witzel data set. It contains the five (out of seven) best ALMA observations with average uncertainty of $\sigma_{\rm obs}^{\rm low} = 4$ mJy. At $\tau \sim 200$ s, the value of the structure function $\mathcal{SF}$ becomes greater than $\sim 3\sigma_{\rm obs}^{\rm high}$, where $\sigma_{\rm obs}^{\rm high} = 13$ mJy is the observational uncertainty of the higher-noise part of the Murchikova & Witzel data set. For 200 s $< \tau <$ 2000 s, we use their entire data set to calculate $\mathcal{SF}$. The 2000 s threshold is set where we start to become limited by statistics and is equal to about one-half the length of the ALMA execution, $\sim$70 minutes/$2 = 35$ minutes $\simeq$ 2000 s. At this timescale, we only have 14 independent samples of this length in the high-cadence data.

On long timescales, between 1400 s (about 25 minutes) and 11,000 s (190 minutes), we use a combination of the Witzel et al. (2021) and Dexter et al. (2014) data sets. The lower threshold is determined by the timescale at which the value of the structure function calculated from the data is greater than the few sigmas of the observational uncertainties per data set used. The upper threshold is chosen such that data points from at least two telescopes are present and that there are about 10 independent data stretches of length τ in each of these telescopes.

To construct the average structure function on timescales 25 minutes $\leqslant \tau \leqslant$ 190 minutes, we calculate the $\mathcal{SF}$ using Equation (1) for data from each telescope individually and then average them. The total lengths (with gaps removed) of the ALMA and SMA data sets in Witzel et al. (2021) and the SMA and CARMA data sets in Dexter et al. (2014) are about $\sim$2000 minutes; therefore, we average the structure functions with identical weights. We choose this averaging to preserve the physical meaning of the structure function, which is the offset of the flux value $F(t+\tau)$ from $F(t)$. This approach also allows us to avoid high-variability and high-noise measurements (particularly CARMA) dominating the result.

The long-timescale (25 minutes $\leqslant \tau \leqslant$ 190 minutes) part of the $\mathcal{SF}$ is constructed using data sets observed during multiple epochs between 2009 and 2017. It is a better epoch-sampled data set than the one dominating the structure function on short timescales ($\tau <$ 2000 s $\simeq$ 35 minutes). Our normal approach would be to construct the long-timescale part of the observational structure function and then renormalize the short-timescale part in such a way that it is matched with the long-timescale one. However, the long-timescale data is strongly influenced by data from the long-decommissioned CARMA telescope, which is the noisiest and the most variable data set available. If we remove the CARMA data set, then to align the short-timescale $\mathcal{SF}$ with the long-timescale part we need to multiply the short-timescale $\mathcal{SF}$ by a factor of 0.95. If we keep the CARMA data set, we will have to multiply the short-timescale $\mathcal{SF}$ by 1.15.

To avoid the CARMA sample dominating our results, we renormalize long-timescale part of the $\mathcal{SF}$ in such a way that it matches the short-timescale part. To this end, the long-timescale (25 minutes $\leqslant \tau \leqslant$ 190 minutes) part of the $\mathcal{SF}$ is multiplied by a factor of 0.87 to make it aligned with the short-timescale ($\tau <$ 2000 s $\simeq$ 35 minutes) part of the structure function. If we remove the CARMA data set, the long-timescale part of $\mathcal{SF}$ has to be multiplied by a factor of 1.05 to align with the short-timescale part. Both sets of points are plotted in Figure 3. The shapes of the curves with and without the CARMA data set are identical.

We observe a general trend in the Sgr A* structure functions calculated with different parts of the data sets: The shapes of the $\mathcal{SF}$ (within the range of timescales τ where the results are statistically reliable) are the same but offset from each other by a constant multiplicative factor varying from observation to observation.

3. Simulations

The simulations we use are all evolved with `Athena++` (Stone et al. 2020), using its ideal general-relativistic magnetohydrodynamics (GRMHD) capabilities (White et al.

2016). Here we provide details in terms of the gravitational length $r_g = GM/c^2$ and time $t_g = GM/c^3$. In case of the Sgr A* black hole, the gravitational length is about 0.04 au and the gravitational time is about 20 s.

3.1. SANE Torus

For the SANE case, we use the aligned simulation first described in White et al. (2020), similar to the standard SANE models studied in the literature and compared in Porth et al. (2019). The black hole has dimensionless spin $a = 0.9$, and the initial conditions are a prograde hydrodynamic equilibrium torus from Fishbone & Moncrief (1976) with the inner edge at $r_{in} = 15\, r_g$ and the pressure maximum at $25\, r_g$. The fluid is taken to have an adiabatic index of $\Gamma = 4/3$. An initial poloidal magnetic field is added to the torus, normalized such that the density-weighted average of the plasma β^{-1} (the ratio of magnetic pressure p_{mag} to thermal pressure) is 0.01.

The simulation coordinates are spherical Kerr–Schild, where three levels of static mesh refinement beyond the root grid achieves an effective resolution of $448 \times 256 \times 352$ cells in radius, polar angle, and azimuthal angle within 50° of the midplane. Radial spacing is logarithmic (239 cells per decade), running from inside the horizon to $r = 100\, r_g$.

The simulation is evolved to a time of $t = 11{,}000 t_g$, reaching inflow equilibrium beyond $r = 20 r_g$. Only data past $5000 t_g$ is used for this analysis. The dimensionless magnetic flux ϕ saturates between 7 and 17 in Gaussian units, well below the MAD regime of approximately 47 (Tchekhovskoy et al. 2011). After fixing the density scale in order to match the overall observed submm flux (see Section 4), the average density in the innermost $10 r_g$ is 2×10^{-17} g cm^{-3}.

3.2. MAD Torus

For the MAD case, we employ a standard $a = 0.9375$ MAD torus simulation like those commonly studied in the literature (e.g., McKinney et al. 2012). The initial Fishbone & Moncrief (1976) torus has an inner radius of $r_{in} = 20 r_g$ and a pressure maximum of $41 r_g$. The initial magnetic field is set via the vector potential $A_\varphi \propto \max(q, 0)$, with

$$q = \frac{\rho}{\rho_{max}} \left(\frac{r}{r_{in}} \right)^3 \sin^3(\theta) \exp\left(-\frac{r}{400\ r_g} \right) - 0.2, \qquad (2)$$

where ρ is the fluid-frame mass density, $\rho_{max} = 1$, and the proportionality constant is set so that the maximum thermal pressure in the torus divided by the maximum of p_{mag} in the torus is 100.

Small perturbations are added to the initial torus pressure at the 2% level. The adiabatic index for this simulation is $\Gamma = 13/9$. The simulation is evolved for $10{,}000 t_g$, with the last $5000 t_g$ used for analysis, where inflow equilibrium is established out to at least $20 r_g$. Here, the density within $10 r_g$ of the center is 4–5 $\times 10^{-19}$ g cm^{-3}.

3.3. MAD Stellar Winds

Finally, we consider the two stellar-wind simulations from Ressler et al. (2020). Both of these model accretion onto a nonspinning black hole of $\Gamma = 5/3$ matter sourced by realistic winds from the approximately 30 Wolf–Rayet stars nearest to the Galactic Center. While the orbits and mass-loss rates of these stars are well known, the magnetic structure of their winds is more uncertain. One simulation assumes the plasma β_w of the winds is 10^2; the other assumes less magnetization with $\beta_w = 10^6$. Here, β_w is defined as the ratio of ram pressure ρv^2 to p_{mag} in the wind.

These simulations use Cartesian Kerr–Schild coordinates. The root grid extends to $1600\, r_g$ in each direction, with 128^3 cells. Nine nested levels of static mesh refinement are added, with 128^3 cells covering the inner $(6.25\ r_g)^3$ at the highest level.

Both wind-fed simulations are run for a time of $20{,}000 t_g$, with a steady-state region (defined by an accretion rate independent of radius) extending to approximately $35–40 r_g$. The latter $10{,}000 t_g$ is used in this analysis. Both cases result in MAD flows, with $40 \lesssim \varphi \lesssim 60$. The density inside $r = 10 r_g$, set by the known stellar winds themselves, averages 4.5×10^{-19} g cm^{-3} ($\beta_w = 10^2$) and 4.2×10^{-19} g cm^{-3} ($\beta_w = 10^6$).

4. Extracting Submm Variability from Simulated Data

For all simulations, we use the general-relativistic ray-tracing code `grtrans` (Dexter & Agol 2009; Dexter 2016) to produce 230 GHz images from simulation snapshots. These images account for polarized synchrotron emission, absorption, and rotation/conversion. Each image is made with 256^2 pixels covering a field of view of $24 r_g$ (120 μas) on each side, where we take the black hole to have mass $M = 4.152 \times 10^6\, M_\odot$ and to be at a distance of 8.178 kpc (Gravity Collaboration et al. 2019). Only a ~5% change would be induced by instead using the values obtained by Do et al. (2019): a mass of $3.964 \times 10^6\, M_\odot$ and a distance of 7.946 kpc. Integrating the intensity over an image yields a simulated light-curve data point.

For the stellar-wind models, the ray-tracing camera is positioned to correspond with the line of sight from Earth. We use the last 1000 simulation snapshots, spaced by $10 t_g$ (200 s) and thus covering a time of 56.8 hr. Though ideal GRMHD simulations are scale free (the fluid density, fluid pressure, and magnetic field strength can all be scaled up or down consistently with one another), these simulations fix this degree of freedom by knowing the absolute mass-loss rates from the Wolf–Rayet stars. The only freedom we have in generating images is our choice of how electron temperature (which is not important for the hydrodynamics but critical for synchrotron radiation) is determined from the total fluid temperature and other variables. We use the standard prescription from Mościbrodzka et al. (2016), which sets the ion-to-electron temperature ratio based on the plasma β:

$$\frac{T_i}{T_e} = \frac{R_{low} + \beta^2 R_{high}}{1 + \beta^2}. \qquad (3)$$

We fix $R_{low} = 1$ and tune R_{high} until the average flux is 2.4 Jy, finding reasonable values of 23 ($\beta_w = 10^2$) and 9.2 ($\beta_w = 10^6$).

We use a similar procedure for the torus simulations, though in these cases we have more degrees of freedom. Without knowing the orientation (if any) of angular momentum around Sgr A*, the viewing angle is a free parameter, and so we make images from both 5° and 45° off the gas angular momentum (and black hole spin) axis. Additionally, we must choose a physical scale for the model. For this, we fix $R_{high} = 16$ (intermediate between the two stellar-wind values) and adjust the physical scale independently for each viewing angle until the average flux is again 2.4 Jy. For these simulations, we use

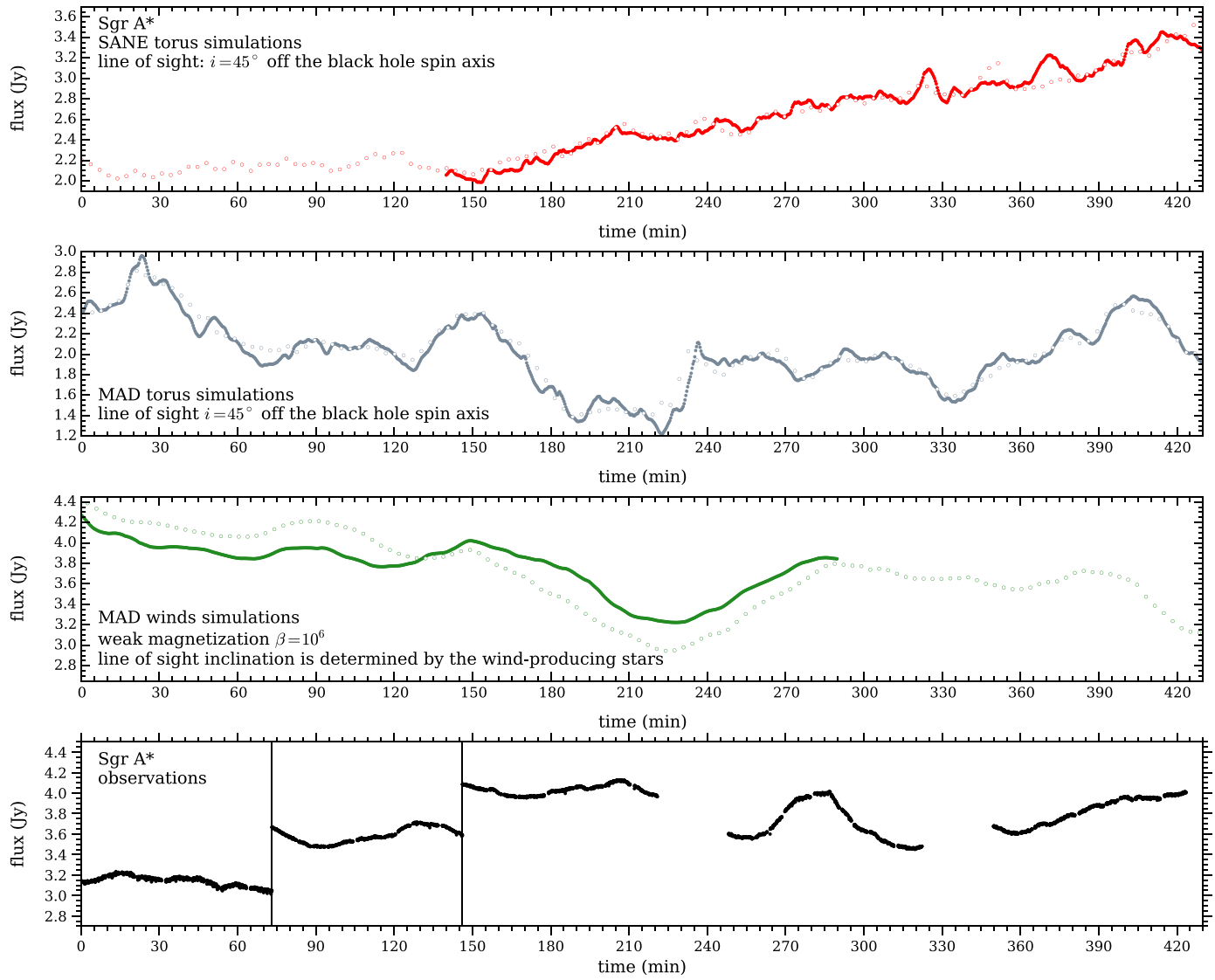

Figure 1. Sgr A*'s simulated and observed light curves. Excerpts from simulated data for the SANE torus, MAD torus, and MAD winds are plotted in red, gray, and green, respectively. Solid points represent finely sampled high-cadence light curves, and empty points represent coarsely sampled data obtained with the fast-light approximation (Section 4). Excerpts from observational data are plotted in black—the sample of ALMA data for project 2018.1.01124.S observed in 2019 June. The total length of the simulated data is about 30 hr for torus models and 56 hr for wind models. The total length of the observational data from all sources used here is greater than about 100 hr.

the last 601 (SANE) or 501 (MAD) snapshots, again separated by $10t_g$ in time, covering 34.1 hr and 28.4 hr, respectively.

The ray-tracing we have discussed so far employs the fast-light approximation, where a single-simulation snapshot is used to make an image, assuming no quantities change while light propagates through the system. Though this is adequate for timescales roughly $10t_g$ or longer, light-curve properties (especially variability) on shorter timescales might be influenced by the fact that the emitting matter is moving at relativistic speeds and so cannot be stationary over a light-crossing time. We therefore also generate images from high-cadence simulation dumps ($\Delta t = 1t_g = 20$ s), employing the slow-light capability of `grtrans`, which uses multiple dumps simultaneously to account for the evolution of the simulation while photons are propagating. We keep the tuned physical scaling and $R_{\rm high}$ values already found. In this way, we produce high-cadence light curves with 852 (SANE torus), 4852 (MAD torus), and 851 (MAD wind) samples, covering 4.8, 27.6, and 4.8 hr, respectively. Excerpts from the resulting light curves are presented in Figure 1.

To obtain the variability structure functions from model light curves, we combine the structure functions calculated using Equation (1) for coarsely and finely sampled data independently. The coarsely sampled light curves are generally longer and consequently better sample the absolute amplitude. Moreover, slow-light calculations require the camera not to be too far from the source (lest the calculation become prohibitively expensive), possibly missing some (essentially constant) emission originating from larger radii. Thus, we multiply the fine-sampling structure function by a coefficient $c_{\rm fine}$ to align it with the coarse-sampling structure function. The alignment coefficients are as follows: For the SANE torus with $i = 5^\circ$ or 45°, $c_{\rm fine} = 0.9$ or 0.78, respectively; for the MAD torus with the same inclinations, $c_{\rm fine} = 0.86$ or 0.8; for the MAD winds, $c_{\rm fine}$ is either 1.2 ($\beta_{\rm w} = 10^2$) or 0.94 ($\beta_{\rm w} = 10^6$).

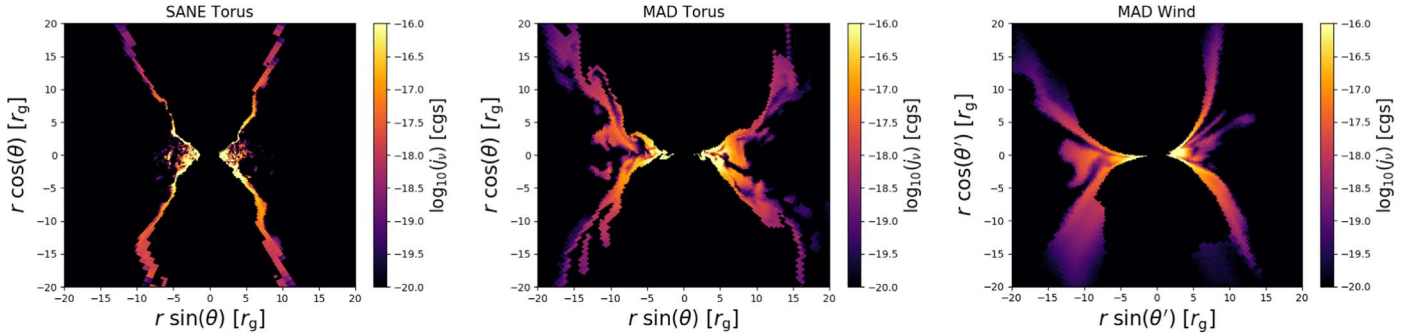

Figure 2. Approximate 230 GHz synchrotron emissivity, j_ν, calculated using Equation (57) of Leung et al. (2011) for the three simulations used in this work. Regions with plasma $\sigma \equiv 2p_{\rm mag}/(\rho c^2) > 1$ are assigned zero emissivity. We reorient the angle of viewing such that the flows are similarly aligned; in all cases, the average direction of the angular momentum vector is pointing upward. Left: SANE torus simulation. Middle: MAD torus simulation. Right: $\beta_{\rm w} = 10^2$ MAD winds simulation. Both MAD simulations have more extended emitting regions than the SANE torus simulation. Furthermore, the MAD torus displays more small-scale turbulence in the emitting regions than the MAD winds. The light curves in Figure 3 reflect these differences, with both MAD simulations displaying longer-term variations than the SANE simulation. Additionally, the MAD winds light curve is much smoother than the other light curves because of the comparative lack of small-scale turbulence.

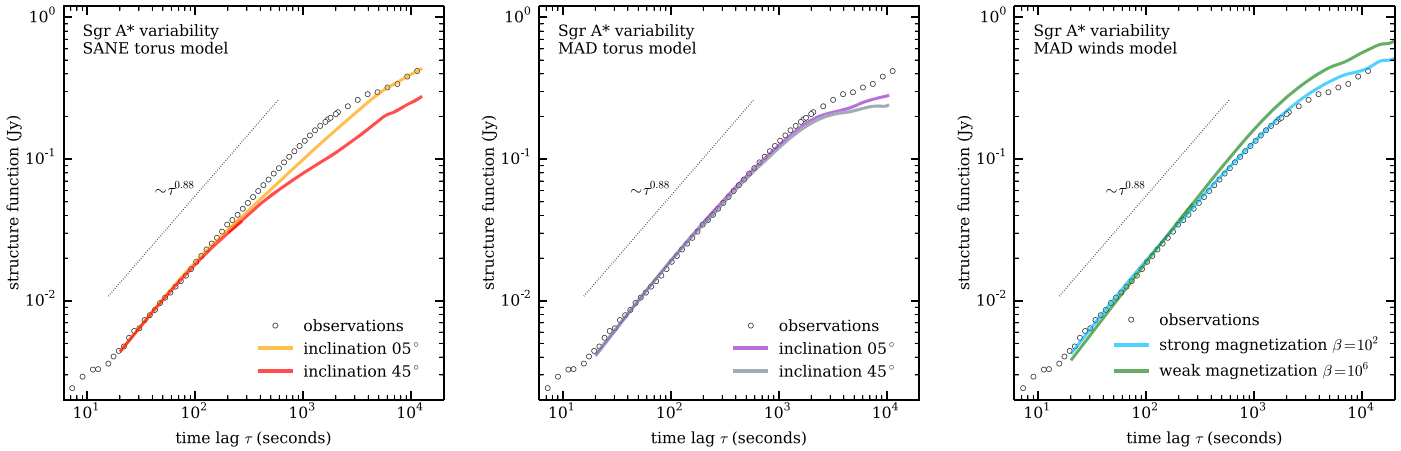

Figure 3. Variability structure function of Sgr A* at 230 GHz. Comparison of simulations and observations. The structure function obtained from observed light curves is depicted with empty black circles. Left: simulations of the SANE Sgr A* accretion flow with torus initial conditions as seen from 5° (yellow) and from 45° (red) off the spin axis of the black hole. Middle: simulations of the MAD Sgr A* accretion with torus initial conditions as seen from 5° (purple) and from 45° (gray) off the spin axis of the black hole. Right: MAD stellar-wind-fed Sgr A* accretion simulations with strong magnetization $\beta_{\rm w} = 10^2$ (blue) and weak magnetization $\beta_{\rm w} = 10^6$ (green) of the stellar winds. The simulated structure functions are normalized by coefficients $c_{\rm comb}$ to align with the observed values. The coefficients are as follows: For the SANE torus, $c_{\rm comb} = 0.72$ ($i = 5°$) or 0.6 ($i = 45°$); for the MAD torus, 0.45 or 0.4 for the same inclinations; for the MAD winds, $c_{\rm comb} = 0.7$ ($\beta_{\rm w} = 10^2$) or 1.15 ($\beta_{\rm w} = 10^6$).

To determine whether the orientation of the flow in the case of the MAD winds model significantly affects the appearance of the light curves and the structure functions, we conduct an inclination test. For the $\beta_{\rm w} = 10^6$ MAD wind simulation, we mock-observe the black hole from both the physical viewing angle (determined by the stellar-wind feeding) and at an artificial 45° inclination. We find that this change has a negligible effect on the structure function.

5. Discussion

By-eye comparison of the simulated and observed light curves in Figure 1 leads us to conclude that the stellar-wind-fed accretion model (MAD winds) produces light curves much closer in shape to the observed one, compared to either the SANE torus or the MAD torus. The typical snapshot of the flow of a MAD wind looks smoother and less stochastic than other analyzed models (Figure 2).

To quantify the variability properties we use the structure function $\mathcal{SF}(\tau)$ defined by Equation (1). The physical meaning of this quantity is the rms of the deviation of the black hole flux between moments in time separated by τ. The comparison of the models with the observational data is presented in Figure 3.

At small timescales, all our structure functions follow the power-law slope of $\sim \tau^{0.88}$. This is close to the universal slope of $\sim \tau^{1.0}$ derived in Appendix. The universal slope, $\mathcal{SF} \sim \tau^{1.0}$, appears when we study the structure function behavior on timescales much smaller than the smallest period of oscillations of the electromagnetic emission in the source. The closeness of the observed index 0.88–1.0 indicates that this condition is nearly met.

The fact that the power-law slope is 0.88 and not 1.0 indicates that weak modes with short periods are present in the data. This is particularly interesting in the case of timescales of about 10 s, which is shorter than the time it takes light to circle halfway around the black hole as fast as possible (via the prograde photon orbit), 6–16$t_{\rm g}$ = 130–330 s, depending on the spin. Such short timescales might arise naturally from brief bursts of emission from small-scale turbulence, though this is less applicable to the wind-fed models (Figure 2). They may be indicative of relativistic velocities moving emitting regions across parts of the domain that are highly magnified by gravitational lensing.

Figure 3 shows that the simulated model structure functions trace the observed one with different degrees of success. The SANE torus model deviates from the observed curve for $\tau \gtrsim 150$ s (2.5 minutes, which is comparable to the light-crossing time). The MAD torus model successfully traces the observations until $\tau \approx 1000$ s (about 15 minutes, which is comparable to the period of the innermost-stable orbit) while the slope remains $\sim \tau^{0.88}$. The observed slope starts gently flattening at larger τ; however, the simulated structure function flattens much faster, and thus deviates substantially.

The MAD winds are the most successful models. The simulated curves trace the observed structure function almost perfectly. They follow the observed slope $\sim \tau^{0.88}$ until about 1000 s, then flatten as gently as in the observations. The model with a strong magnetization of the stellar winds at the source ($\beta_w = 10^2$) does particularly well, tracing the observed structure function between 20 s (the shortest cadence in our simulations) all the way to about 200 minutes.

The fact that the structure function produced by the MAD winds model follows the observed Sgr A* structure function between 20 s and 200 minutes demonstrates that the properties of the light curves in the model and the physical system are similar. In particular, the harmonics influencing the source variability on these timescales are nearly identical. Deviation of the structure functions produced by the SANE torus and MAD torus models from the observed curve on shorter timescales strongly indicates the presence of modes with shorter periods, which are absent in the observations of Sgr A* (see Appendix). These higher-frequency variations are connected to smaller-scale turbulence, as evident from the 2D contour maps of the 230 GHz emissivity shown in Figure 2. Note that the shape of the structure function is influenced by the distribution of these harmonics, their phase shifts, and their relative strengths, while the absolute value of the structure function is also sensitive to the absolute strengths.

The SANE torus, MAD torus, and MAD winds models are evolved using `Athena++` with the same underlying plasma physics. The crucial difference is in the initial conditions and the resulting black hole feeding mechanism. Torus models feed the back hole by initializing a torus on the scale of tens to hundreds of gravitational radii, with the understanding that after sufficient evolution and inside a sufficiently small radius, the resulting accretion disk will be in a quasi-steady state that is independent of the details of those initial conditions. However, the physical system cannot so easily forget the initial property of all material moving on circular orbits with the same orientation of angular momentum. In contrast, the MAD wind simulations include fluid parcels with eccentric orbits with many different orientations, reaching a qualitatively different quasi-steady state and resulting in near-direct-infall feeding. Crucially, it is the latter case that reflects, by construction, the actual feeding of gas in the Galactic Center from ∼30 Wolf–Rayet stars.

We note that torus simulations in the literature can vary in terms of what initial angular momentum profile (Penna et al. 2013) or adiabatic index (White et al. 2020) is assumed, affecting the radial profiles found in steady state, and indeed different adiabatic indices are used in the simulations studied here. However, at least when looking at accretion rate as a function of time, variability does not seem particularly sensitive to this latter parameter (Bollimpalli et al. 2020). We expect that torus simulations with no source of low-angular-momentum gas accreting before circularizing will always be distinguishable in variability from wind-fed simulations with such material.

It is evident that the black hole accretion flow must be sensitive to the precise feeding mechanism. When we take care to include realistic feeding in simulations, the predicted 230 GHz emission reproduces the observed variability of Sgr A* (as in the third and the fourth panels in Figure 1). Standard torus models, on the other hand, predict 230 GHz variability that is too noise like (i.e., high frequency, low amplitude), with short-timescale variability not seen in the observations (as in the first and second panels in Figure 1). Torus models may still play an important role in parameterizing aspects of accretion flows for numerical experiments. For example, as the GRMHD community builds a larger repository of simulations, including tilted tori and tori augmented with low-angular-momentum gas, we will be able to discern the most relevant aspects of wind-fed accretion affecting submm variability.

One possible concern with our analysis is that the wind-fed simulations have been, at least at larger radii, evolved for much longer times than the torus simulations because they include the results of intermediate-scale MHD simulations with duration $> 10^5 t_g$, while the torus simulations last only $\leqslant 11{,}000 t_g$. Because the deviation in the $\mathcal{SF}$. for the latter simulations occurs particularly at large timescales, one might argue that the agreement between the observations and the wind-fed simulations is mostly a product of there being a larger radial range in inflow equilibrium. Indeed, we do find that $\dot{M}$ is approximately constant out to slightly larger radii in the wind-fed simulations than the torus simulations, reaching ≈ 35–$40 r_g$ in the latter and $\approx 20 r_g$ in the former. However, the SFs calculated from a small part of the data at both early and late times in the wind-fed simulation have approximately the same shapes despite the "equilibrium radius" being smaller by $\sim 6 r_g$. We are therefore reasonably confident that the wind-fed simulations' structure functions are not merely reflecting long run times. This also makes sense because most of the 230 GHz emission is concentrated at radii $\lesssim 20 r_g$ (Figure 2). In fact, the deviations from observations correspond to lags of ∼200 s (SANE) to ∼2000 s (MAD), which match Keplerian periods at the horizon and innermost-stable-orbit scales, well inside where inflow equilibrium is established in any model. Particularly long torus simulations may be worth investigating, though we do not expect significant changes to our findings, and it would be surprising for such simulations' light curves to resemble the wind-fed model shown in Figure 1.

Wind-fed GRMHD modeling of black hole accretion at horizon scales is relatively new, and there is a need for further exploration of these sorts of flows with additional simulations, especially given how well they can match the statistical properties seen in Sgr A*. One parameter we have not fully explored here is that of spin. Currently, the spin of Sgr A* is essentially unconstrained, and our two wind-fed models assume the black hole is nonspinning. Future work can vary the magnitude and direction of the spin, especially if forthcoming Event Horizon Telescope resolved images narrow the allowed parameter space.

Taking into account other sources of accreting gas, such as the minispiral and circumnuclear disk in the Galactic Center (Genzel et al. 2010), would also lead to further improvement in the accuracy of the numerical models. In general, we expect

that the better we model the actual feeding of gas onto the Galactic Center black hole (Solanki et al., in preparation), the more realistic will be the behavior obtained in simulations.

Beyond matching the particulars of Sgr A*, wind-fed models are worth investigating in order to catalog the ways in which they differ from the torus-initialized simulations that have dominated the literature to date. Stellar winds may be applicable to many low-luminosity supermassive black hole accretion flows. Even without resolved images, we have demonstrated here that light-curve statistics can distinguish between these classes of models.

6. Conclusions

We compare the observed variability of the Sgr A* black hole at about 230 GHz with those generated by three classes of theoretical models for the accretion flow at horizon scales. We rely on the structure function to compare the statistical properties of the light curves. This allows us to compare variability properties without being concerned with particular realizations of stochastic processes.

We consider three types of accretion flow models: SANE torus, MAD torus, and MAD winds. The first two types are torus-initialized models with either a small amount of accreted net magnetic flux or a significant coherent accreted magnetic flux, respectively. The last type consists of stellar-wind-fed models informed by realistic feeding of material onto the black hole by nearby Wolf–Rayet stars. It also results in an MAD accretion flow.

We find that our stellar-wind-fed models match Sgr A* variability properties much better than either of the torus-initialized models. They produce light curves visually similar to the observed ones, in stark contrast with more noise-like torus-model light curves. The variability properties of these light curves, quantified with the structure function on a timescale between 20 s and 200 minutes, are nearly identical to those obtained from observational data. This demonstrates that the harmonics and their relative strengths influencing the source variability on these timescales are nearly identical to the ones present in Sgr A*. By contrast, the structure functions of the SANE torus and MAD torus models show that they are affected by the presence of modes with shorter periods, which are absent in the observations of Sgr A*.

The crucial difference between the wind-fed and torus-initiated models is the structure of the accretion flow near the black hole. In the case of the torus models, the material is strongly circularized by the initial setup and undergoes many orbits before eventually accreting into the black hole. In this scenario, the higher-frequency modes affecting variability are likely connected to instabilities and smaller-scale turbulence that has many orbits to develop, leading to more noise-like light curves. In the case of stellar-wind models, the structure of the accretion flow near the black hole is closer to direct infall, leaving nearly no time for instabilities to develop and dramatically affect the submm emission, thus resulting in smoother light curves. These smooth light curves are very similar to the observed one, indicating that the Sgr A* feeding is better described by stellar-wind feeding. This, perhaps, is not a surprising conclusion.

In our analysis, we used no parameter tuning to achieve such an excellent match (other than choosing $R_{\rm high}$ so that the 230 GHz flux $\approx$2.4 Jy). In general, stellar-wind-fed models have much less room for after-the-fact parameter tuning than torus models; the fact that any choice of $R_{\rm high}$ can reproduce the observed amount of Galactic Center horizon-scale synchrotron emission is itself very much nontrivial.

This work leads us to two primary conclusions. First, we have demonstrated that wind-fed models can be distinguished from torus-fed models. This can be done without resolved images of the accretion flow. In fact, it is not a priori guaranteed that time-averaged images of these models are observationally different. Therefore, studying time variability is complementary to image analysis and gives us another way to distinguish between the torus-fed and wind-fed models.

Second, our analysis demonstrates that the wind-fed models are more appropriate for Sgr A* than those that are fed by tori. If wind-fed plasma circularizes at large-enough distances, it is possible that it would mimic torus-fed plasma in the innermost regions, where all 230 GHz emission is produced. Thus, a key property of our Sgr A* wind-fed models (and thus by inference the Galactic Center accretion flow itself) is that the gas does not circularize at large radii, as discussed in Ressler et al. (2020). If the parcels of plasma in the inner tens of $r_{\rm g}$ do indeed have the broad distribution of angular momenta (i.e., inclinations and eccentricities) that results from stochastic feeding by multiple wind sources rather than the narrow distribution provided by a torus, then certain properties of the accretion flow may never match models that consider only torus initializations. If torus models are to be made to match observations, adding features (e.g., a supply of low-angular-momentum gas) informed by wind-fed simulations may well be necessary.

We are grateful to the anonymous referees for perceptive and useful comments.

L.M. acknowledges the support of William D. Loughlin and Corning Glass Foundation memberships at the Institute for Advanced Study. S.M.R. was supported by the Gordon and Betty Moore Foundation through grant GBMF7392. This research was supported in part by the National Science Foundation (NSF) under grant No. NSF PHY-1748958.

This paper makes use of the following ALMA data: ADS/JAO.ALMA#2018.1.01124.S. ALMA is a partnership of ESO (representing its member states), NSF (USA) and NINS (Japan), together with NRC (Canada) and NSC and ASIAA (Taiwan) and KASI (Republic of Korea), in cooperation with the Republic of Chile. The Joint ALMA Observatory is operated by ESO, AUI/NRAO and NAOJ.

The National Radio Astronomy Observatory is a facility of the National Science Foundation operated under cooperative agreement by Associated Universities, Inc.

This work used the Extreme Science and Engineering Discovery Environment (XSEDE) clusters Stampede2 (at the Texas Advanced Computing Center, TACC, through allocations AST170012 and AST200005) and Comet (at the San Diego Supercomputing Center, SDSC, through allocation AST090038), as well as the Princeton Research Computing cluster Stellar managed and supported by the Princeton Institute for Computational Science and Engineering (PICSciE) and the Office of Information Technology's High Performance Computing Center and Visualization Laboratory at Princeton University. Finally, this work made use of computing time granted by UCB on the Savio cluster.

Software: `grtrans` (Dexter & Agol 2009; Dexter 2016), `Athena++` (White et al. 2016; Stone et al. 2020).

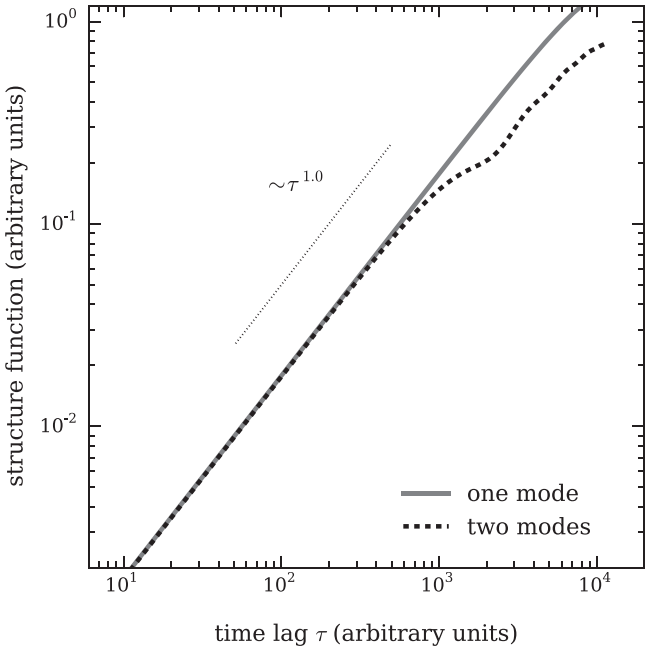

Figure 4. Structure functions of simple harmonics sources described by Equation (A3). Solid line: single-mode source with $A = 1$, $\omega = 2\pi/50{,}000$, $B = \nu = 0$. Dashed line: two-mode source with the same A, ω as above and $B = 0.15$, $\nu = 2\pi/5000$. The $\mathcal{SF}$ is multiplied by the factor of 0.55 to align with single-mode $\mathcal{SF}$. Universal scaling $\sim \tau^{1.0}$ is plotted with a dotted line.

Appendix
Structure Functions of Simplest Harmonic Sources

Let us calculate the structure function of a source of a single-frequency harmonic emission: $F(t) = A\sin(\omega t)$. We find that

$$\mathcal{SF}^2(\tau) = \frac{A^2}{T-\tau}\int_0^T dt(\sin(\omega(t+\tau)) - \sin(\omega t))^2 = 2A^2\sin^2(\omega\tau), \quad \text{(A1)}$$

$$\mathcal{SF}(\tau) = \sqrt{2}A|\sin(\omega\tau)|. \quad \text{(A2)}$$

Here, ω is the frequency of the source, A the amplitude of the signal, and T the duration of the light curve analyzed. We assume that the timescale on which we study variability is much shorter than the length of the data $\tau \ll T$ and that $T \gg 2\pi/\omega$.

We see that at short timescales $\tau \to 0$, the structure function has a scaling $\mathcal{SF} \sim \tau$. This can be proven for a general flux $F(t) = \int F(\omega)e^{i\omega t}d\omega$ with a high-frequency cutoff ω_0 and any $\tau \ll 1/\omega_0$.

Let us calculate the structure function emission with two distinct frequencies: $F(t) = A\sin(\omega t) + B\sin(\nu t + \beta)$. We find

$$\mathcal{SF}(\tau) = \sqrt{2}\,[A^2\sin^2(\omega\tau) + B^2\sin^2(\nu\tau)]^{1/2}. \quad \text{(A3)}$$

Here we also assume that the two frequencies are distinct and that length of the light curve is such that $T \gg 1/(\omega - \nu)$.

In Figure 4 we show examples of a structure function of one- and two-harmonic sources, plotted on the same scale as the observed and simulated structure functions in Figure 3. The period of a dominant mode is 50,000 s (about 14 hr) and the period of the subdominant mode is 5000 s (83 minutes). The subdominant harmonic has an amplitude of 0.15 times that of the dominant harmonic. We see that both structure functions trace the universal slope of $\sim \tau^{1.0}$ at small timescales. Then at about 500 s, the two-mode structure function starts deviating from the one-mode case (which continues tracing the universal slope almost perfectly). This deviation is caused by the presence of the lower-frequency subdominant harmonic (Figure 4). We choose the parameters in Figure 4 in such a way that the two-mode structure function deviates from the one-mode one at about the same timescale as the SANE torus $\mathcal{SF}$ deviates from the MAD winds $\mathcal{SF}$ (left panel in Figure 3).

We conclude that the deviation of the structure functions obtained from simulated SANE torus and MAD torus light curves from the observed ones on short timescales (Figure 3) implies the presence in the numerical models of the emission oscillation modes with shorter periods than in the observed system. Comparison with Figure 4 illustrates this.

We choose the period of the dominant mode at about 14 hr to ensure there is no turn-down behavior of the one- and two-mode structure function within the range of τ plotted. The fact that the required period is similar to the 8 hr variability period suggested by Dexter et al. (2014) was unexpected.

ORCID iDs

Lena Murchikova https://orcid.org/0000-0001-8986-5403
Sean M. Ressler https://orcid.org/0000-0003-0220-5723

References

Bollimpalli, D. A., Mahmoud, R., Done, C., et al. 2020, MNRAS, 496, 3808
Dexter, J. 2016, MNRAS, 462, 115
Dexter, J., & Agol, E. 2009, ApJ, 696, 1616
Dexter, J., Kelly, B., Bower, G. C., et al. 2014, MNRAS, 442, 2797
Do, T., Hees, A., Ghez, A., et al. 2019, Sci, 365, 664
Event Horizon Telescope Collaboration, Akiyama, K., Alberdi, A., et al. 2019, ApJL, 875, L1
Fishbone, L. G., & Moncrief, V. 1976, ApJ, 207, 962
Genzel, R., Eisenhauer, F., & Gillessen, S. 2010, RvMP, 82, 3121
Gravity Collaboration, Abuter, R., Amorim, A., et al. 2019, A&A, 625, L10
Gravity Collaboration, Abuter, R., Amorim, A., et al. 2020, A&A, 638, A2
Leung, P. K., Gammie, C. F., & Noble, S. C. 2011, ApJ, 737, 21
McKinney, J. C., Tchekhovskoy, A., & Blandford, R. D. 2012, MNRAS, 423, 3083
Mościbrodzka, M., Falcke, H., & Shiokawa, H. 2016, A&A, 586, A38
Murchikova, L., & Witzel, G. 2021, ApJL, 920, L7
Neilsen, J., Markoff, S., Nowak, M. A., et al. 2015, ApJ, 799, 199
Penna, R. F., Kulkarni, A., & Narayan, R. 2013, A&A, 559, A116
Porth, O., Chatterjee, K., Narayan, R., et al. 2019, ApJS, 243, 26
Ressler, S. M., Quataert, E., & Stone, J. M. 2020, MNRAS, 492, 3272
Ressler, S. M., White, C. J., Quataert, E., & Stone, J. M. 2020, ApJL, 896, L6
Stone, J. M., Tomida, K., White, C. J., & Felker, K. G. 2020, ApJS, 249, 4
Tchekhovskoy, A., Narayan, R., & McKinney, J. C. 2011, MNRAS, 418, L79
White, C. J., Dexter, J., Blaes, O., & Quataert, E. 2020, ApJ, 894, 14
White, C. J., Quataert, E., & Gammie, C. F. 2020, ApJ, 891, 63
White, C. J., Stone, J. M., & Gammie, C. F. 2016, ApJS, 225, 22
Witzel, G., Martinez, G., Willner, S. P., et al. 2021, ApJ, 917, 73